Volume 9 | Number 7 | 7 April 2025

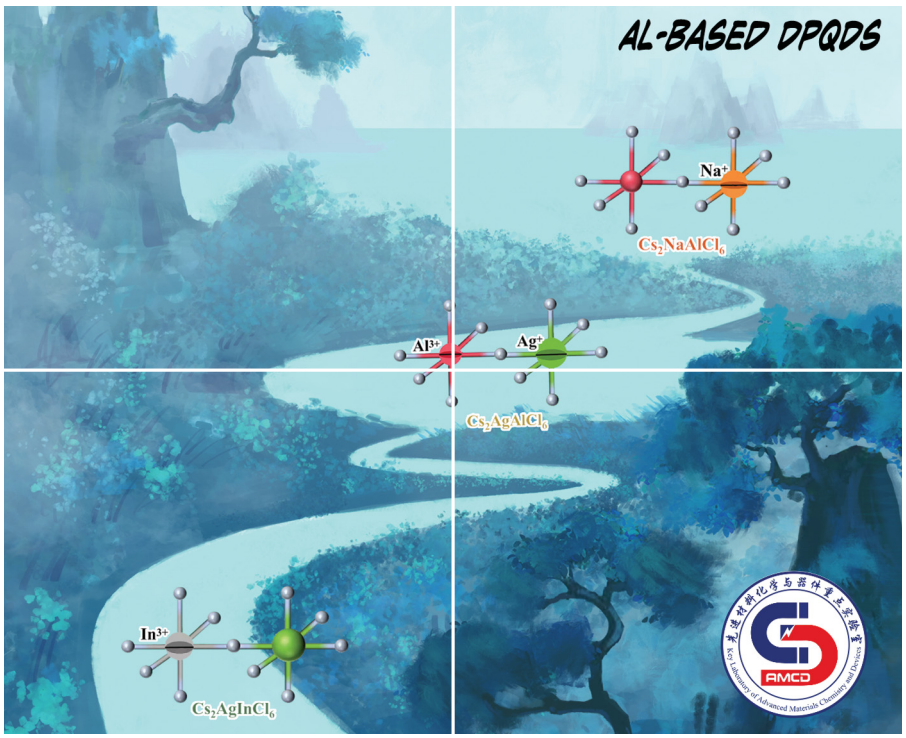

MATERIALS CHEMISTRY

FRONTIERS

CCS 中国化学会 CHINESE CHEMICAL SOCIETY
ICCAS
ROYAL SOCIETY OF CHEMISTRY
rsc.li/frontiers-materials

MATERIALS CHEMISTRY FRONTIERS

RESEARCH ARTICLE

View Article Online
View Journal | View Issue

Cite this: *Mater. Chem. Front.*, 2025, **9**, 1118

Synthesis and luminescence of Al based double perovskite quantum dots†

Liyuan Zhang,‡ Chasina Wang‡ and Chuanlang Zhan *

Direct-bandgap AgIn based non-lead double perovskite quantum dots (DPQDs) face the challenge of low photoluminescence quantum yields (PLQYs). To address this issue, approaches such as ion doping and surface passivation have been developed, by which both emission color and intensity have been modulated. In this article, we selected ($r_{Al^{3+}}$ = 0.053) to replace In^{3+} ($r_{In^{3+}}$ = 0.081 nm) and further used Na^+ (r_{Na^+} = 0.098 nm) to replace Ag^+ (r_{Ag^+} = 0.126 nm), resulting in the synthesis of two new types of non-doped DPQDs, *i.e.* $Cs_2AgAlCl_6$ and $Cs_2NaAlCl_6$. The synthesized Al-based DPQDs have a hexagonal polycrystalline structure with average sizes of 8.84 nm and 5.76 nm, respectively. X-ray diffraction (XRD) data indicate the lattice contraction of $Cs_2AgAlCl_6$ and $Cs_2NaAlCl_6$ DPQDs in comparison to $Cs_2AgInCl_6$. X-ray photoelectron spectroscopy (XPS) data indicate the presence of all four elements Cs, Ag/Na, Al and Cl in the QDs. Compared with $Cs_2AgInCl_6$ DPQDs, replacement of In^{3+} with Al^{3+} increases the PLQY from 1.5% to 7.4% and further to 8.5% when Ag^+ is further replaced with Na^+. Doping the $Cs_2AgAlCl_6$ and $Cs_2NaAlCl_6$ DPQDs with Bi^{3+} ions further increases the PLQYs to 10.1% and 11.4%, respectively. The PLQY of $Cs_2AgAlCl_6$ DPQDs is again increased to 10.9% with the use of a ligand mixture of *n*-trioctylphosphine : oleylamine (40% : 60%). Our results demonstrate that the replacement of In^{3+} with small radius Al^{3+} is an effective strategy to enhance the emission of non-doped pristine direct-bandgap DPQDs and open an avenue for designing new types of DPQDs.

Received 7th November 2024,
Accepted 7th January 2025

DOI: 10.1039/d4qm00967c

rsc.li/frontiers-materials

1. Introduction

Lead halide perovskite materials have many unique physicochemical properties, including higher light absorption coefficients and defect tolerance, longer carrier diffusion lengths, higher carrier mobilities, and potential ferroelectricity, which have injected new vitality into chemistry, materials science, and physics, and added a new chapter to the history of optoelectronic devices.[1–7] However, the toxicity of lead (Pb) and the poor stability of these materials to light, heat, water, and oxygen have hindered their advancement.[8–13] Therefore, lead-free perovskite materials with lower toxicity and higher stability have attracted much interest.[14–16] A promising strategy to solve the lead toxicity problem is to replace every two divalent Pb^{2+} cations with a monovalent cation and a trivalent cation to form charge-ordered double perovskites with the general formula $A_2B(I)B(III)X_6$.

Double perovskite materials exhibit two types of semiconducting properties, *i.e.* indirect bandgap and direct bandgap. Common indirect bandgap double perovskite materials include $Cs_2AgBiCl(Br)_6$ and $Cs_2AgSbCl(Br)_6$. Participation of phonons in the electronic transition processes leads to lower absorption coefficients and photoluminescence quantum yields (PLQYs).[17–21] In contrast, In-based direct bandgap DPQDs such as $Cs_2AgInCl_6$ and $Cs_2NaInCl_6$ exhibit higher absorption coefficients, long carrier lifetimes and facile solution processability. In-based DPQDs were first reported in 2017.[22] Subsequently, extensive research has been conducted on their synthesis, composition modification, electronic structure, optoelectronic properties, and applications. However, this type of DPQDs still encounters the problem of parity-forbidden transitions, which in turn leads to a lower PLQY, typically below 2%. Several approaches such as ion doping and surface passivation have been developed to enhance the emission.[23–27]

Doping of ions enables tuning of the crystal structure and hence the emission mechanisms. Recently, in the field of indirect bandgap double perovskites, Chen *et al.*[28] doped $Cs_2AgBiCl_6$ with Na^+, which has a smaller ionic radius than Ag^+, and it was found that the bond length of the Bi^{3+}–Cl^- connected to the neighbouring sodium ions was shortened from 0.2717 nm to 0.2696 nm, which in turn reduced the local site symmetry of Bi^{3+}, thus facilitating the absorption and

Key Laboratory of Advanced Materials Chemistry and Devices (AMCDLab) of the Department of Education of Inner Mongolia Autonomous Region, College of Chemistry and Environmental Science, Inner Mongolia Normal University, Huhhot 010022, China. E-mail: clzhan@imnu.edu.cn

† Electronic supplementary information (ESI) available. See DOI: https://doi.org/10.1039/d4qm00967c

‡ These authors contributed equally.

excitation of Bi^{3+}, and improving the PLQY of Ln^{3+} ions. Jadkar *et al.*[29] doped $Cs_2AgBiCl_6$ with Fe^{3+}, which has a smaller ionic radius than Bi^{3+} ions to enhance its PL strength to 10 times that of the original. The lattice constants were found to decrease with more Fe^{3+} doping by density functional theory (DFT) calculations. This indicates that the doping of Fe^{3+} with a smaller radius causes its lattice to shrink and the symmetry to be broken, thereby increasing the luminescence intensity of $Cs_2AgBiCl_6$. In the field of direct bandgap double perovskites, Chen *et al.*[28] similarly doped Na^+, which has a smaller ionic radius than Ag^+, into $Cs_2AgInCl_6$, and the symmetry of the $AgCl_6$ octahedron is broken, leading to enhanced luminescence. Luo *et al.*[30] doped Na^+ into the $Cs_2AgInCl_6$ double perovskite and observed breaking of the inversion symmetry of the lattice structure and change of the electronic wave function of Ag^+ sites from symmetry to asymmetry. This led to odd–even variations in the self-trapped exciton (STE) wave function, allowing for radiative recombination.

Lessons from ion doping indicate that a modulation of the crystal structure with doping cations having different ionic radii can be a way to enhance the emission of DPQDs. Currently, In^{3+} is generally used to act as trivalent metal ions to construct direct-bandgap DPQDs. However, as stated above, the non-doped pristine In^{3+} based DPQDs exhibit very low PLQYs. Research studies on ion doping have clearly indicated that ion doping, when the host–guest metal ions have different radii, will induce lattice shrinkage, hence changing the luminescence mechanisms and leading to increased PLQYs. In this context, we hypothesize: if the In^{3+} ion can be replaced with another metal ion that has a larger or smaller radius, can it induce lattice shrinkage and enhance the emission? To verify this, we herein focus on Al^{3+} because (1) Al is in the same group as In and this will allow us to obtain a direct bandgap for the as-synthesized Al-based DPQDs and (2) with Al^{3+} having a smaller radius than In^{3+} ($r_{Al^{3+}}$ = 0.053, $r_{In^{3+}}$ = 0.081 nm), if In^{3+} successfully replaced with Al^{3+}, lattice shrinkage will be induced.

Practically, with $Cs_2AgInCl_6$ as the model DPQDs, we began our research. First, we calculated the tolerance factor and octahedral factor. The calculated tolerance factor is 0.92, which is within the region of 0.8–1.0, and the octahedral factor is 0.49, being in the range of 0.4–0.9. The values of both factors guarantee the formation of a stable double perovskite structure when replacing In^{3+} with Al^{3+} (Fig. 1a and b). Second, we attempted to synthesize $Cs_2AgAlCl_6$ QDs, and luckily the synthesis was successful. Then, we further replaced Ag^+ with Na^+ and successfully synthesized $Cs_2NaAlCl_6$ QDs. The synthesized DPQDs have a hexagonal polycrystalline structure with average sizes of 8.84 nm and 5.76 nm, respectively, and the X-ray diffraction (XRD) data indicate lattice shrinkage and X-ray photoelectron spectroscopy (XPS) data indicate that they contain four elements, *i.e.* Cs, Ag/Na, Al and Cl. Measurements indicate that the PLQY is enhanced from 1.5% for $Cs_2AgAlCl_6$ to 7.4% for $Cs_2AgAlCl_6$ and further to 8.5% for $Cs_2NaAlCl_6$ (Fig. 1c). A huge increase in the PLQY is thus obtained with our strategy.

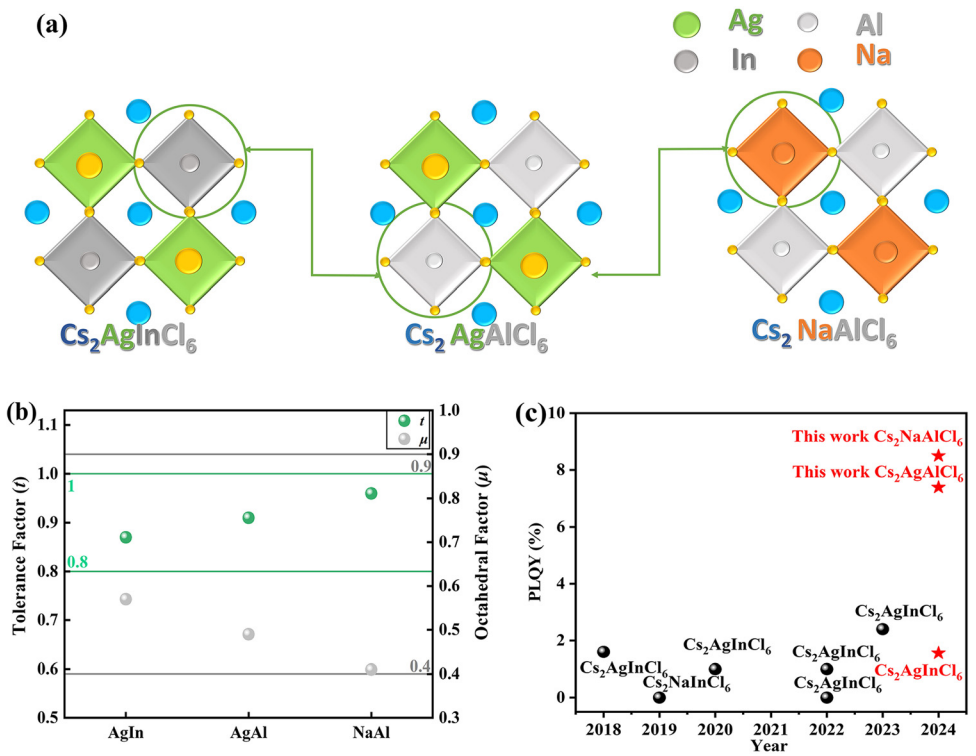

Fig. 1 (a) Concept of designing $Cs_2AgAlCl_6$ and $Cs_2NaAlCl_6$ QDs. (b) The values of the tolerance factor and octahedral factor of $Cs_2AgInCl_6$, $Cs_2AgAlCl_6$ and $Cs_2NaAlCl_6$ DPQDs. (c) Distributions of the PLQYs of the DPQDs with direct bandgaps.

2. Results and discussion

2.1 Design and DFT calculations

The Goldschmidt tolerance factor (t) and octahedral factor (μ)[31] are usually used to measure whether a structure could form a stable perovskite. The t-value and μ-value are calculated using formulas (1) and (2), respectively. The r_B value is calculated using formula (3), where r_A, r_B, $r_{B^{1+}}$, $r_{B^{3+}}$, and r_X represent the ionic radii of components A, B, B^{1+}, B^{3+}, and X, respectively. Generally, when the t-value is between 0.80 and 1.00 and the μ-value is between 0.40 and 0.90, it can be determined that the components can form a stable perovskite structure. The tolerance factor and octahedral factor of $Cs_2AgInCl_6$, $Cs_2AgAlCl_6$ and $Cs_2NaAlCl_6$ QDs were calculated to prove that they could form stable double perovskite structures (Fig. 1b).

$$t = \frac{r_A + r_X}{\sqrt{2}(r_B + r_X)} \quad (1)$$

$$\mu = \frac{r_B}{r_X} \quad (2)$$

$$r_B = \frac{r_{B^{1+}} + r_{B^{3+}}}{2} \quad (3)$$

The calculated values of t/μ of $Cs_2AgInCl_6$, $Cs_2AgAlCl_6$ and $Cs_2NaAlCl_6$ are 0.87/0.57, 0.92/0.49, and 0.97/0.41, respectively (Fig. 1b), indicating that all of them enable the formation of stable double perovskite structures.

The crystal structures of the three DPQDs were optimized *via* the density functional theory (DFT) method. The calculated bond lengths and angles are collected in Table 1. For $Cs_2AgInCl_6$ and $Cs_2AgAlCl_6$, the bond angles of Cl–Ag–Cl, Cl–In–Cl, and Cl–Al–Cl remain at 180° and 90° and those of Ag–Cl–In and Ag–Cl–Al at 90°, which means both the $[AgCl_6]^{5-}$ and $[InCl_6]^{3-}$ form a perfect octahedron (Fig. 2). From In^{3+} to Al^{3+}, the radius of B^{3+} ions decreases from 0.081 nm to 0.053 nm. The calculated bond length of B^{3+}–Cl^- decreases from 0.256 nm for In^{3+}–Cl^- to 0.236 nm for Al^{3+}–Cl^-, and the bond length of Ag^+–Cl^- increases slightly. As a result, the tetrahedron length as indicated by the distance of B^+–B^{3+} decreases from 0.527 nm for $Cs_2AgInCl_6$ to 0.513 nm for $Cs_2AgAlCl_6$ (Fig. 2), indicating enhanced interactions between the Cs^+ and the surrounding $[AgCl_6]^{5-}$ and $[InCl_6]^{3-}$ octahedrons.

Further replacement of Ag^+ with Na^+ yields $Cs_2NaAlCl_6$. The radii of Ag^+ and Na^+ are 0.126 nm and 0.098 nm, respectively.

In $Cs_2NaAlCl_6$, perfect octahedrons are also formed (Fig. 2), as indicated by the bond angles of Cl–Na–Cl, Cl–Al–Cl and Na–Cl–Al. The bond length of Al–Cl further decreases to 0.235 nm and the bond length of Na–Cl increases to 0.286 nm. The tetrahedral length as indicated by the distance of B^+–B^{3+} decreases to 0.515 nm (Fig. 2).

Table 1 Summary of the bond lengths and bond angles of $Cs_2AgInCl_6$, $Cs_2AgAlCl_6$ and $Cs_2NaAlCl_6$ QDs simulated from DFT calculations

	Bond length (nm)		Bond angle (°)		
$Cs_2AgInCl_6$	Ag–Cl 0.272	In–Cl 0.256	Cl–Ag–Cl 180/90	Cl–In–Cl 180/90	Ag–Cl–In 90
$Cs_2AgAlCl_6$	Ag–Cl 0.277	Al–Cl 0.236	Cl–Ag–Cl 180/90	Cl–Al–Cl 180/90	Ag–Cl–Al 90
$Cs_2NaAlCl_6$	Na–Cl 0.286	Al–Cl 0.235	Cl–Na–Cl 180/90	Cl–Al–Cl 180/90	Na–Cl–Al 90

2.2 Synthesis

The synthetic route is developed by modifying the synthesis of non-doped $Cs_2AgInCl_6$ reported by Qu *et al.*[32] In the synthesis of $Cs_2AgAlCl_6$ and $Cs_2NaAlCl_6$, stoichiometric amounts of metal carboxylate precursors (*i.e.* $Al(OAc)_3$, AgOAc NaOAc, and CsOAc) and the ligands oleic acid and oleylamine (OA and OAm) were dissolved in the non-polar solvent octadecene (ODE) at 110 °C under a nitrogen atmosphere. Then the chlorine source, *e.g.* TMS-Cl, was injected immediately when the temperature rose to 155 °C, which immediately formed a precipitate of

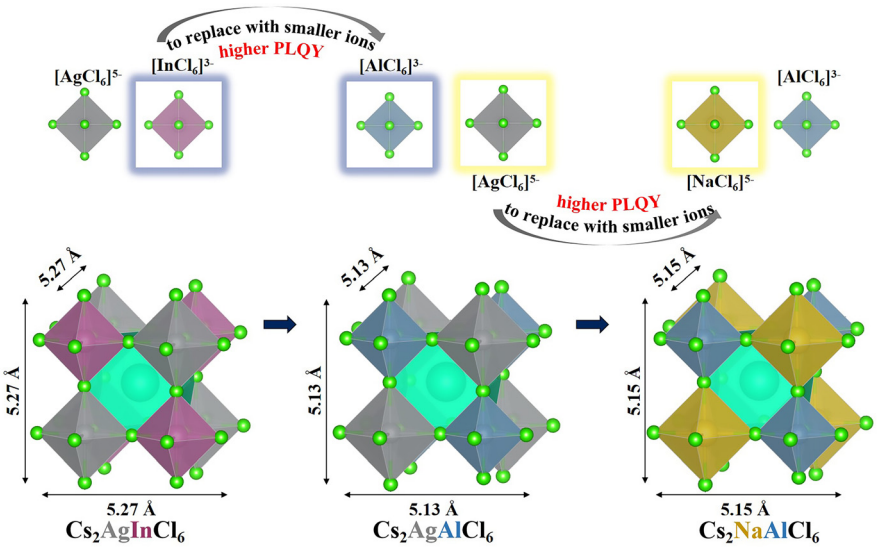

Fig. 2 Structural diagrams of $Cs_2AgInCl_6$, $Cs_2AgAlCl_6$ and $Cs_2NaAlCl_6$ QDs observed from the [100] crystal plane.

$Cs_2AgAlCl_6$ and $Cs_2NaAlCl_6$. The mixture was kept for 30 s at 155 °C for completion of reaction. Then it was immediately subjected to an ice bath and cooled to room temperature. Finally, the precipitate was centrifuged and dispersed in *n*-hexane, affording the DPQDs. Details of synthesis and characterization methods are given in the ESI.†

2.3 Structural characterizations

The XRD patterns of $Cs_2AgInCl_6$, $Cs_2AgAlCl_6$, and $Cs_2NaAlCl_6$ QDs are given in Fig. 3. The characteristic diffraction peaks observed at 2θ of 22°, 31°, 39°, 44°, and 55° are related to 022, 222, 224, 004, and 620 crystal planes. The presence of these characteristic peaks confirms the formation of the perovskite structures of the $Cs_2AgAlCl_6$ and $Cs_2NaAlCl_6$ QDs[33] (Fig. 3). The diffraction peaks related to 222, 224, 004 and 620 planes shift to the higher 2θ direction in comparison to the diffractions from the $Cs_2AgInCl_6$ QDs, which is consistent with the theoretical calculation results, *i.e.* the tetrahedra are shrunk.

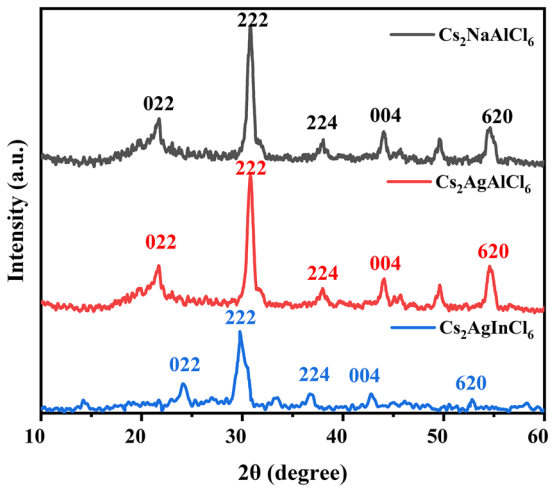

Fig. 3 XRD patterns of $Cs_2AgAlCl_6$, $Cs_2NaAlCl_6$ and $Cs_2AgInCl_6$ QDs.

The transmission electron microscopy (TEM), high resolution transmission electron microscopy (HRTEM) and selected area electron diffraction (SAED) images of $Cs_2AgAlCl_6$ and $Cs_2NaAlCl_6$ QDs are shown in Fig. 4. The $Cs_2AgAlCl_6$ and $Cs_2NaAlCl_6$ QDs show a homogeneous hexagonal shape, and their average sizes are about 8.84 nm and 5.76 nm, respectively. The HRTEM images show that they both appear to be uniformly lattice-striped, and the (022) lattice constant of the crystal plane is 0.37 nm, which is consistent with the previously reported $Cs_2AgInCl_6$ QDs.[34] The polycrystalline nature of the double perovskite structure is confirmed by SAED patterns revealing the presence of diffraction rings on the (022) and (004) crystal faces of both QDs.

To further determine the elemental species of $Cs_2AgAlCl_6$ QDs, elemental analyses were performed using XPS. The full spectrum of $Cs_2AgAlCl_6$ QDs is shown in Fig. S1a (ESI†), which contains the characteristic peaks of Cs 3d, Ag 3d, Al 2p, and Cl 2p. The characteristic peaks of Ag in its fine spectrum (Fig. 5a) appear at 368 eV and 374 eV, corresponding to the spin–orbit coupling of Ag $3d_{5/2}$ and $3d_{3/2}$, respectively. The characteristic peaks of Al in its fine spectrum (Fig. 5b) appear at 77 eV and 75 eV, which correspond to the spin–orbit coupling of Al $2p_{1/2}$ and $2p_{3/2}$, respectively. This proves that Al has

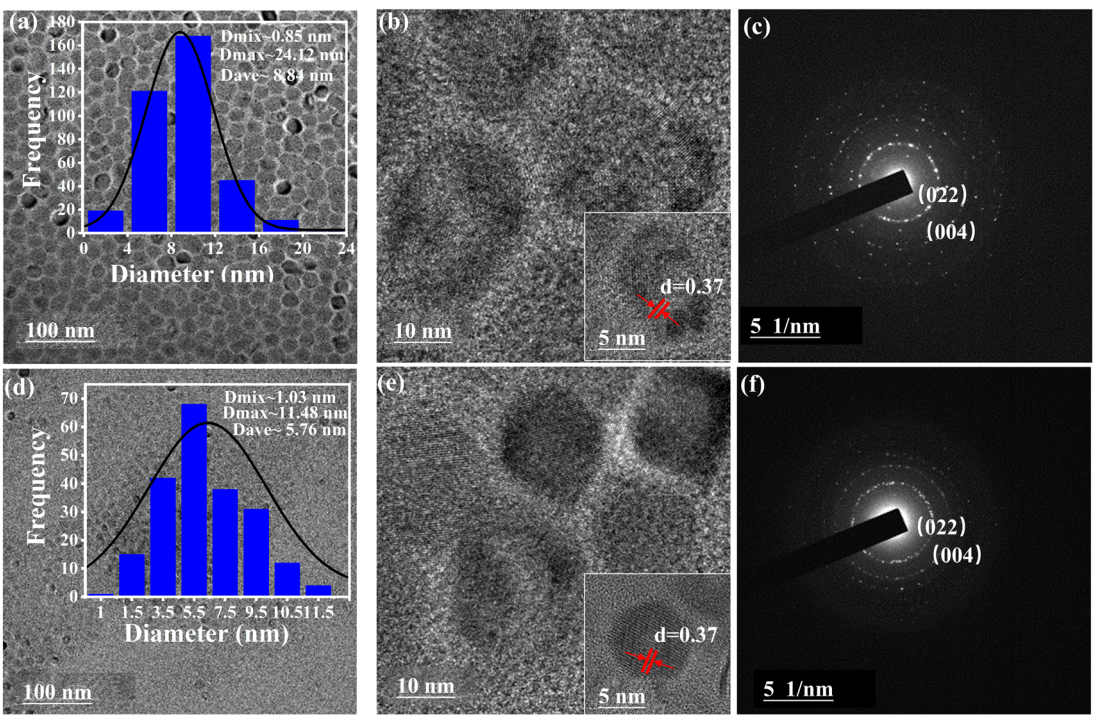

Fig. 4 (a)–(c) The TEM, HRTEM and SAED images of $Cs_2AgAlCl_6$ QDs. (d)–(f) The TEM, HRTEM and SAED images of $Cs_2NaAlCl_6$ QDs.

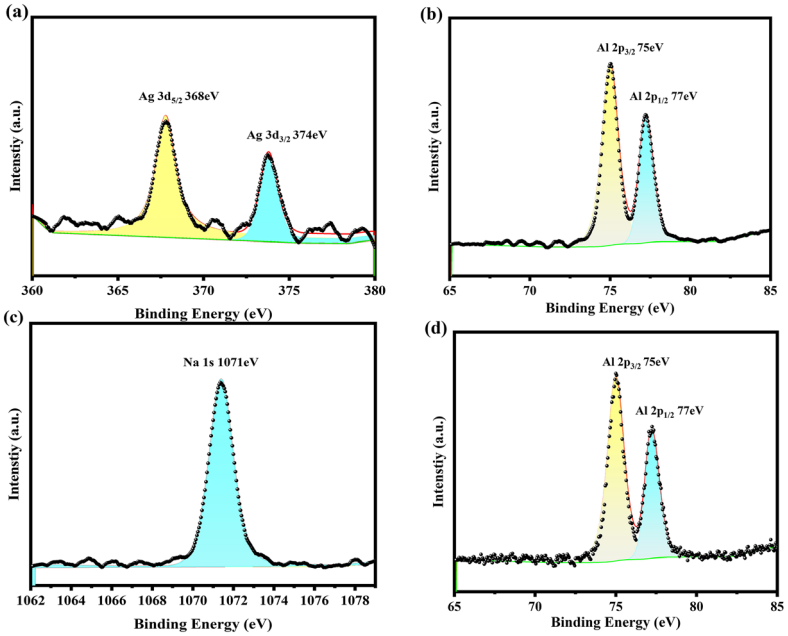

Fig. 5 $Cs_2NaAlCl_6$ and $Cs_2NaAlCl_6$ QDs: (a)–(d) XPS fine spectra corresponding to Ag 3d, Na 1s, and Al 2p, respectively.

successfully participated in the composition of $Cs_2AgAlCl_6$ QDs. The fine spectra of the other elements are shown in Fig. S1 (ESI†). Similarly, the XPS spectra of the $Cs_2NaAlCl_6$ QDs (Fig. S2a, ESI†) clearly show the characteristic peaks of Cs 3d, Na 1s, Al 2p, and Cl 2p, and its fine spectrum of Na (Fig. 5c) shows a characteristic peak of Na 1s at 1071 eV, which corresponds to the 1s orbital of Na. This proves that Na has successfully participated in the composition of $Cs_2NaAlCl_6$ QDs. Similarly, the fine spectrum of Al is given in Fig. 5d. The fine spectra of the other elements are shown in Fig. S2 (ESI†).

2.4 Luminescence performance

To further understand the luminescence properties of $Cs_2Ag/NaAlCl_6$ QDs, we first characterized the absorption spectrum of the two newly synthesized DPQDs, which are shown in Fig. 6a. The absorption of $Cs_2AgInCl_6$ QDs is also given in Fig. 6a for comparison, which shows characteristic absorption features regarding the In^{3+} based direct bandgap DPQDs, *i.e.* two absorption shoulders observed around 267 nm and 310 nm. At 267 nm, the band edge has opposite parity, allowing for transitions and exhibiting relatively strong absorption.[22] There are no obvious changes in the absorption with the group IIIA elements changing from In to Al.

The excitation maxima of the $Cs_2Ag/NaAlCl_6$ QDs appear around 373 nm, which is similar to the excitation maximum observed for the $Cs_2AgInCl_6$ QDs. Again, the luminescence peaks of $Cs_2Ag/NaAlCl_6$ QDs appear around 450 nm and they are also similar to the emission observed from the $Cs_2AgInCl_6$ QDs. The similarity of absorption, excitation and luminescence spectra shown in Fig. 6a further confirms the successful synthesis of the $Cs_2Ag/NaAlCl_6$ QDs.

For the two newly synthesized DPQDs, the emission peak is observed at 449 nm for $Cs_2AgAlCl_6$ QDs and 446 nm for $Cs_2NaAlCl_6$ QDs. The blue-shift of the emission peak is consistent with the smaller size observed from the TEM image (Fig. 4) when the Ag^+ is replaced with Na^+. The full width at half maximum (FWHM) is 102 nm with a Stokes shift of 183 nm for $Cs_2AgAlCl_6$ QDs and is 104 nm with a Stokes shift of 179 nm for $Cs_2NaAlCl_6$ QDs. Emission with a broad FWHM and a large Stokes shift is a typical characteristic of STE emission.[35,36]

The PLQYs of $Cs_2AgAlCl_6$ and $Cs_2NaAlCl_6$ QDs were subsequently tested at 373 nm and 371 nm excitation wavelengths, respectively. The values are 7.4% and 8.5%, respectively, which are significantly higher than that of $Cs_2AgInCl_6$ QDs (1.5%) (Fig. S3, ESI†). To further verify its PLQY enhancement, the time-resolved photoluminescence (TR-PL) spectra (Fig. 6b) were measured at 449 nm and 446 nm, respectively, from which the average decay lifetimes were found to be 5.35 ns and 5.43 ns for $Cs_2AgAlCl_6$ and $Cs_2NaAlCl_6$ QDs, respectively, while for $Cs_2AgInCl_6$ QDs, the average lifetime was 4.60 ns. The relatively longer lifetimes are consistent with the increase in the PLQY.

2.5 Ion doping

In order to further enhance the PLQYs of $Cs_2AgAlCl_6$ and $Cs_2NaAlCl_6$ QDs, an ion doping strategy was employed. The commonly used Bi^{3+} ions with an ns^2 electronic configuration were doped into them to modify the bandgap's parity forbidden transition so as to achieve a further improvement in PLQYs.[23] We used the same synthetic method to dope Bi^{3+} into $Cs_2AgAlCl_6$ and $Cs_2NaAlCl_6$ QDs at doping ratios of 20%, 40%, 60%, 80%, and 100%, respectively. To understand the luminescence properties of Bi–$Cs_2Ag/NaAlCl_6$ QDs. We first characterized the absorption spectra of $Cs_2AgAlCl_6$ and $Cs_2NaAlCl_6$ QDs (Fig. 7a and d). Upon doping with Bi^{3+}, absorption peaks at 335 nm and 330 nm are observed, respectively, which indicates that (1) Bi^{3+}

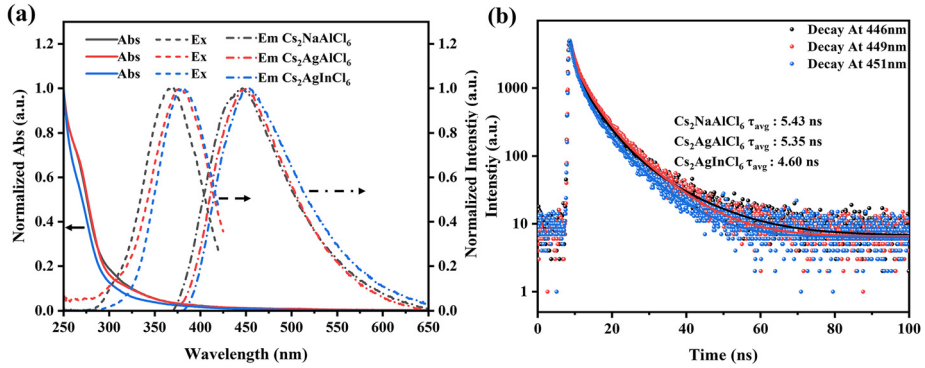

Fig. 6 (a) UV-Vis absorption, steady-state excitation and photoluminescence spectra and (b) TR-PL spectra.

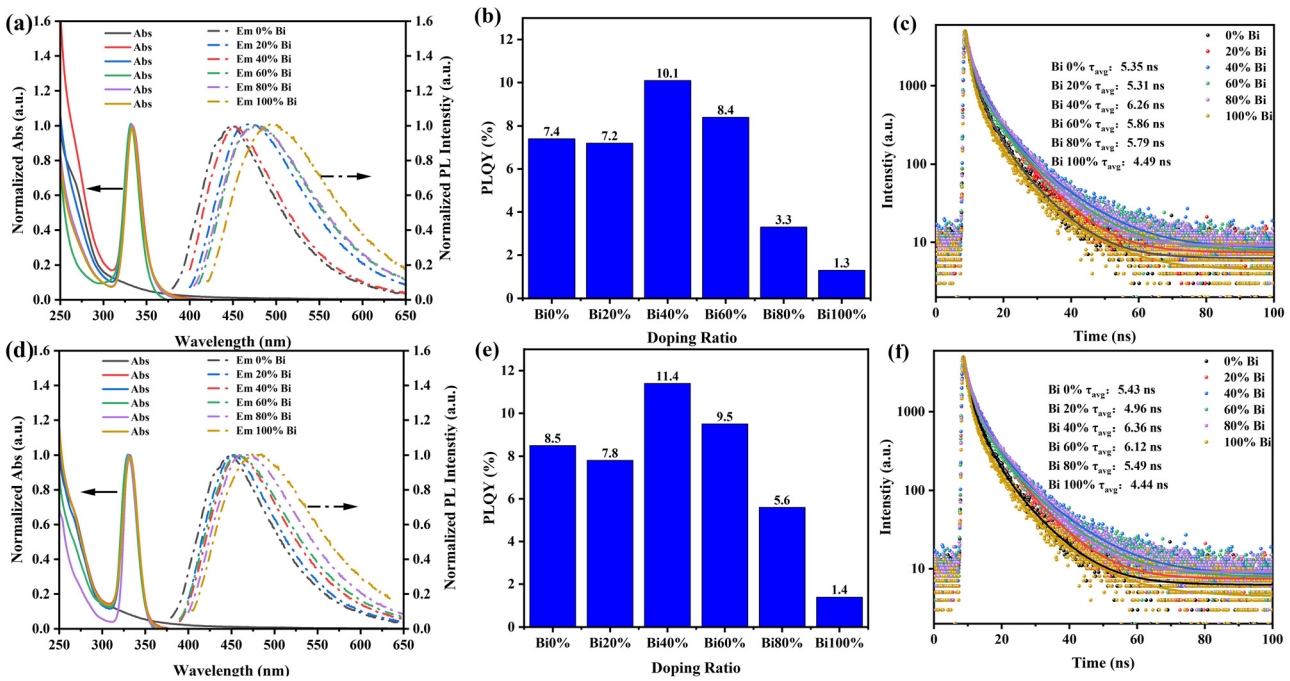

Fig. 7 (a) and (d) UV-Vis absorption and photoluminescence spectra, (b) and (e) PLQYs, and (c) and (f) TR-PL spectra of $Cs_2AgAlCl_6$ (a)–(c) and $Cs_2NaAlCl_6$ (d)–(f) doped with 20%, 40%, 60%, 80% and 100% Bi^{3+} ions, respectively.

has been successfully doped and (2) the doping has successfully broken the parity barrier transition of $Cs_2AgAlCl_6$ and $Cs_2NaAlCl_6$ QDs.

The Bi–$Cs_2AgAlCl_6$ and Bi–$Cs_2NaAlCl_6$ QDs show a broad emission in the range of 380–650 nm, which shows a red-shift (449–494 nm and 446–480 nm) (Fig. 7a and c) with increasing doping ratio. Upon doping with Bi^{3+}, the PLQYs of Bi–$Cs_2AgAlCl_6$ and Bi–$Cs_2NaAlCl_6$ first increase (7.4% to 10.1% and 8.6% to 11.4%) and then decrease (10.1% to 1.3% and 11.3% to 1.4%) with the increase of Bi^{3+} ion doping ratios, and the highest PLQYs of 10.1% and 11.4% are obtained at a doping ratio of 40% (Fig. 7b and e). The enhancement of PLQYs can be due to the fact that Bi^{3+} doping breaks the symmetry and contributes to the PLQY. However, as the Bi^{3+} ion doping ratio increases, the bandgap changes gradually from the direct nature to indirect characteristics, resulting in a decrease in the PLQY.[20]

The TR-PL spectra were measured and are shown in Fig. 7c and f, from which the average decay lifetimes were obtained upon doping with 0%, 20%, 40%, 60%, 80%, and 100% Bi^{3+}. The lifetimes also increase first and then decrease with the increase of the Bi^{3+} ion doping ratio, and the longest lifetimes are observed at a doping ratio of 40% (6.26 ns and 6.36 ns; Fig. 7c and f), which are consistent with the change of the PLQY.

2.6 Ligand passivation

In addition to ion doping modification strategies, researchers also investigated ligand passivation strategies to enhance the PLQYs of DPQDs. Here, we also further adopt commonly used ligand passivation strategies so as to enhance the PLQY. Due to

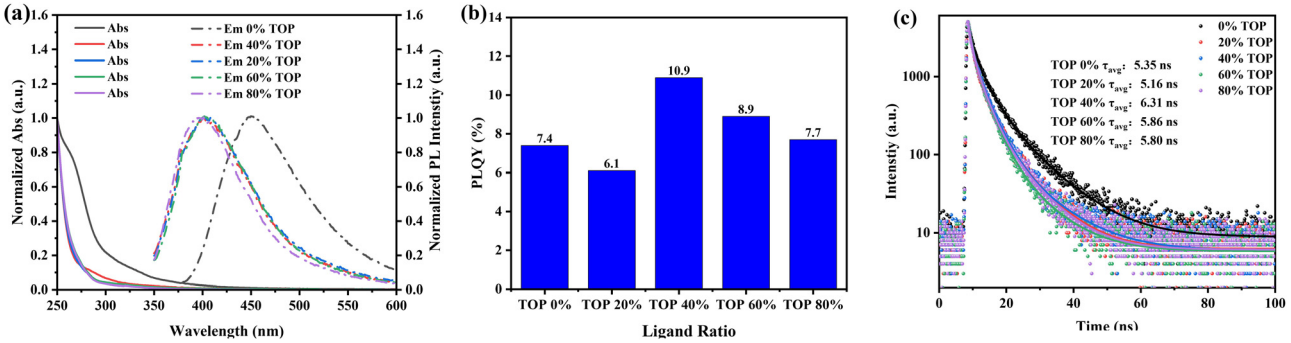

Fig. 8 (a) UV-Vis absorption and photoluminescence spectra, (b) PLQYs, and (c) TR-PL spectra of $Cs_2AgAlCl_6$ with the addition of 20%, 40%, 60%, and 80% TOP to replace the OAm.

the easy detachment of traditional oleic acid and oleylamine (OAm) ligands on the surface of QDs, we selected *n*-trioctylphosphine (TOP), a phosphorus ligand, which has relatively strong coordination with halogen ion defects on the surface of QDs and with surface metal ions to passivate the $Cs_2AgAlCl_6$ QDs. Firstly, TOP was combined with OAm at a ratio of 0%, 20%, 40%, and 80% and a series of TOP-modified $Cs_2AgAlCl_6$ QDs were synthesized. Their absorption and luminescence spectra are given in Fig. 8a. Modifications with TOP lead to a blue-shift in absorption and luminescence, which is consistent with literature reports.[17] The PLQYs are also dependent on the used content of TOP and the highest PLQY with a value of 10.9% was observed at a content of 40% TOP (Fig. 8b). At this TOP ratio, the longest lifetime of 6.31 ns was observed (Fig. 8c).

3. Conclusions

In summary, we report in this paper two new types of direct bandgap DPQDs by replacing the element In with the same group element Al. The smaller radius of Al^{3+} than that of In^{3+} ($r_{Al^{3+}}$ = 0.053, $r_{In^{3+}}$ = 0.081 nm) causes lattice shrinkage and hence significantly enhances the PLQYs of non-doped pristine DPQDs. Through this strategy, we have successfully synthesized two new types of direct bandgap DPQDs, *e.g.* $Cs_2AgAlCl_6$ and $Cs_2NaAlCl_6$ DPQDs, whose PLQYs are 7.4% and 8.5%, respectively, and are significantly higher than the PLQY of the control $Cs_2AgInCl_6$ DPQDs (1.5%). Doping $Cs_2AgAlCl_6$ and $Cs_2NaAlCl_6$ DPQDs with Bi^{3+} (40%) enhances their PLQYs up to 10.1% and 11.4%, respectively. Modifications of the surface of $Cs_2AgAlCl_6$ DPQDs with a mixture of TOP and OAm (40% : 60%) give rise to a PLQY of 10.9%. Our results clearly demonstrate a new strategy to tune the emission mechanisms of the non-doped pristine DPQDs and will be valuable in further designing high-PLQY DPQDs.

Author contributions

Liyuan Zhang: conceptualization, data curation, formal analysis, investigation, methodology, resources, validation, visualization and writing – original draft. Chasina Wang: conceptualization, formal analysis, methodology, visualization and writing – original draft. Chuanlang Zhan: conceptualization, funding acquisition, project administration, supervision, and writing – review & editing.

Data availability

The data supporting this article have been included as part of the ESI.†

Conflicts of interest

There are no conflicts of interest to declare.

Acknowledgements

The authors acknowledge the financial support from the Natural Science Foundation of China (NSFC; No. 22171151 and U23A20593), the Department of Education of Inner Mongolia Autonomous Region, and the Inner Mongolia Normal University (No. 112/1004031962).

References

1 S. Bhalla, D. T. Melnekoff, A. Aleman, V. Leshchenko, P. Restrepo, J. Keats, K. Onel, J. R. Sawyer, D. Madduri and J. Richter, Patient similarity network of newly diagnosed multiple myeloma identifies patient subgroups with distinct genetic features and clinical implications, *Sci. Adv.*, 2021, **7**, eabg9551.
2 S. D. Stranks, G. E. Eperon, G. Grancini, C. Menelaou, M. J. Alcocer, T. Leijtens, L. M. Herz, A. Petrozza and H. J. Snaith, Electron-hole diffusion lengths exceeding 1 micrometer in an organometal trihalide perovskite absorber, *Science*, 2013, **342**, 341–344.
3 M. A. Green, A. Ho-Baillie and H. J. Snaith, The emergence of perovskite solar cells, *Nat. Photonics*, 2014, **8**, 506–514.
4 H. Wu, Y. Ge, G. Niu and J. Tang, Metal halide perovskites for X-ray detection and imaging, *Matter*, 2021, **4**, 144–163.

5 Y. Zhou, J. Chen, O. M. Bakr and O. F. Mohammed, Metal halide perovskites for X-ray imaging scintillators and detectors, *ACS Eenergy Lett.*, 2021, **6**, 739–768.
6 K. Li, H. Lian, R. Van Deun and M. G. Brik, A far-red-emitting $NaMgLaTeO_6$:Mn^{4+} phosphor with perovskite structure for indoor plant growth, *Dyes Pigm.*, 2019, **162**, 214–221.
7 K. Li and R. V. Deun, Obtaining efficiently tunable red emission in $Ca_{3-\delta}Ln_\delta WO_6$: Mn^{4+} (Ln = La, Gd, Y, Lu, δ = 0.1) phosphors derived from nearly nonluminescent Ca_3WO_6: Mn^{4+} *via* ionic substitution engineering for solid-state lighting, *ACS Sustainable Chem. Eng.*, 2020, **8**, 7256–7261.
8 M. D. Smith and H. I. Karunadasa, White-light emission from layered halide perovskites, *Acc. Chem. Res.*, 2018, **51**, 619–627.
9 Y. Kim, E. Yassitepe, O. Voznyy, R. Comin, G. Walters, X. Gong, P. Kanjanaboos, A. F. Nogueira and E. H. Sargent, Efficient luminescence from perovskite quantum dot solids, *ACS Appl. Mater. Interfaces*, 2015, **7**, 25007–25013.
10 A. Jodlowski, D. Rodríguez-Padrón, R. Luque and G. De Miguel, Alternative perovskites for photovoltaics, *Adv. Energy Mater.*, 2018, **8**, 1703120.
11 Z. Deng, F. Wei, S. Sun, G. Kieslich, A. K. Cheetham and P. D. Bristowe, Exploring the properties of lead-free hybrid double perovskites using a combined computational-experimental approach, *J. Mater. Chem. A*, 2016, **4**, 12025–12029.
12 G. Volonakis, M. R. Filip, A. A. Haghighirad, N. Sakai, B. Wenger, H. J. Snaith and F. Giustino, Lead-free halide double perovskites via heterovalent substitution of noble metals, *J. Phys. Chem. Lett.*, 2016, **7**, 1254–1259.
13 F. Giustino and H. J. Snaith, Toward lead-free perovskite solar cells, *ACS Energy Lett.*, 2016, **1**, 1233–1240.
14 X. Wang, T. Zhang, Y. Lou and Y. Zhao, All-inorganic lead-free perovskites for optoelectronic applications, *Mater. Chem. Front.*, 2019, **3**, 365–375.
15 Y. Li, Z. Zhou, N. Tewari, M. Ng, P. Geng, D. Chen, P. K. Ko, M. Qammar, L. Guo and J. E. Halpert, Progress in copper metal halides for optoelectronic applications, *Mater. Chem. Front.*, 2021, **5**, 4796–4820.
16 Y. Wang, J. Ren, X. Zhou and G. Zhang, Stability improvements of metal halide perovskite nanocrystals and their optoelectrical applications, *Mater. Chem. Front.*, 2023, **7**, 2175–2207.
17 G. Volonakis, A. A. Haghighirad, R. L. Milot, W. H. Sio, M. R. Filip, B. Wenger, M. B. Johnston, L. M. Herz, H. J. Snaith and F. Giustino, $Cs_2InAgCl_6$: a new lead-free halide double perovskite with direct band gap, *J. Phys. Chem. Lett.*, 2017, **8**, 772–778.
18 A. H. Slavney, T. Hu, A. M. Lindenberg and H. I. Karunadasa, A bismuth-halide double perovskite with long carrier recombination lifetime for photovoltaic applications, *J. Am. Chem. Soc.*, 2016, **138**, 2138–2141.
19 E. T. Mcclure, M. R. Ball, W. Windl and P. M. Woodward, Cs_2AgBiX_6 (X = Br, Cl): new visible light absorbing, lead-free halide perovskite semiconductors, *Chem. Mater.*, 2016, **28**, 1348–1354.
20 A. Karmakar, G. M. Bernard, A. Meldrum, A. O. Oliynyk and V. K. Michaelis, Tailorable indirect to direct band-gap double perovskites with bright white-light emission: decoding chemical structure using solid-state NMR, *J. Am. Chem. Soc.*, 2020, **142**, 10780–10793.
21 N. Chen, T. Cai, W. Li, K. Hills-Kimball, H. Yang, M. Que, Y. Nagaoka, Z. Liu, D. Yang and A. Dong, Yb-and Mn-doped lead-free double perovskite Cs_2AgBiX_6 (X = Cl^-, Br^-) nanocrystals, *ACS Appl. Mater. Interfaces*, 2019, **11**, 16855–16863.
22 J. Zhou, Z. Xia, M. S. Molokeev, X. Zhang, D. Peng and Q. Liu, Composition design, optical gap and stability investigations of lead-free halide double perovskite $Cs_2AgInCl_6$, *J. Mater. Chem. A*, 2017, **5**, 15031–15037.
23 P. Han and K. Han, Recent advances in all-inorganic lead-free three-dimensional halide double perovskite nanocrystals, *Energy Fuels*, 2021, **35**, 18871–18887.
24 L. Zhang, C. Wang, J. Hu and C. Zhan, Research Progress on Luminescence Performance of Double Perovskite Quantum Dots Regulated by Ion Doping, *Chem. J. Chin. Univ.*, 2024, **45**, 1–15.
25 Y. Liu, A. Nag, L. Manna and Z. Xia, Lead-free double perovskite $Cs_2AgInCl_6$, *Angew. Chem., Int. Ed.*, 2021, **133**, 11696–11707.
26 K. Tosa, C. Ding, S. Chen, S. Hayase and Q. Shen, Classifying the Role of Surface Ligands on the Passivation and Stability of $Cs_2NaInCl_6$ Double Perovskite Quantum Dots, *Nanomaterials*, 2024, **14**, 376.
27 R. Ahmad, L. S. ZdražIl, S. Kalytchuk, A. Naldoni, A. L. Rogach, P. Schmuki, R. Zboril and S. T. P. N. Kment, Uncovering the Role of Trioctylphosphine on Colloidal and Emission Stability of Sb-Alloyed $Cs_2NaInCl_6$ Double Perovskite Nanocrystals, *ACS Appl. Mater. Interfaces*, 2021, **13**, 47845–47859.
28 Y. Pei, D. Tu, C. Li, S. Han, Z. Xie, F. Wen, L. Wang and X. Chen, Boosting near-infrared luminescence of lanthanide in $Cs_2AgBiCl_6$ double perovskites via breakdown of the local site symmetry, *Angew. Chem., Int. Ed.*, 2022, **61**, e202205276.
29 R. Udavant, S. Thawarkar, S. Rondiya, A. Shelke, R. Aher, T. G. Ajithkumar, R. W. Cross, N. Y. Dzade and S. Jadkar, Lead-Free Solid State Mechanochemical Synthesis of $Cs_2NaBi_{1-x}Fe_xCl_6$ Double Perovskite: Reduces Band Gap and Enhances Optical Properties, *Inorg. Chem.*, 2023, **62**, 4861–4871.
30 J. Luo, X. Wang, S. Li, J. Liu, Y. Guo, G. Niu, L. Yao, Y. Fu, L. Gao and Q. Dong, Efficient and stable emission of warm-white light from lead-free halide double perovskites, *Nature*, 2018, **563**, 541–545.
31 Y. Wei, Z. Cheng and J. Lin, An overview on enhancing the stability of lead halide perovskite quantum dots and their applications in phosphor-converted LEDs, *Chem. Soc. Rev.*, 2019, **48**, 310–350.
32 Y. Zhang, Z. Zhang, W. Yu, Y. He, Z. Chen, L. Xiao, J. J. Shi, X. Guo, S. Wang and B. Qu, Lead-free Double Perovskite $Cs_2AgIn_{0.9}Bi_{0.1}Cl_6$ Quantum Dots for White Light–Emitting Diodes, *Adv. Sci.*, 2022, **9**, 2102895.
33 P. Han, X. Mao, S. Yang, F. Zhang, B. Yang, D. Wei, W. Deng and K. Han, Lead-free sodium–indium double perovskite nanocrystals through doping silver cations for bright yellow emission, *Angew. Chem., Int. Ed.*, 2019, **131**, 17391–17395.

34 Y. Liu, Y. Jing, J. Zhao, Q. Liu and Z. Xia, Design optimization of lead-free perovskite $Cs_2AgInCl_6$:Bi nanocrystals with 11.4% photoluminescence quantum yield, *Chem. Mater.*, 2019, **31**, 3333–3339.
35 L. Cao, X. Jia, W. Gan, C. G. Ma, J. Zhang, B. Lou and J. Wang, Strong self-trapped exciton emission and highly efficient near-infrared luminescence in Sb^{3+}–Yb^{3+} Co-doped $Cs_2AgInCl_6$ double perovskite, *Adv. Funct. Mater.*, 2023, **33**, 2212135.
36 W. Van Der Stam, J. J. Geuchies, T. Altantzis, K. H. Van Den Bos, J. D. Meeldijk, S. Van Aert, S. Bals, D. Vanmaekelbergh and C. De Mello Donega, Highly emissive divalent-ion-doped colloidal $CsPb_{1-x}M_xBr_3$ perovskite nanocrystals through cation exchange, *J. Am. Chem. Soc.*, 2017, **139**, 4087–4097.

